Constitutive modeling of deformation behavior of high-entropy alloys with face-centered cubic crystal structure

Min Ji Jang, Dong-Hyun Ahn, Jongun Moon, Jae Wung Bae, Dami Yim, Jien-Wei Yeh, Yuri Estrin & Hyoung Seop Kim

MATERIALS RESEARCH LETTERS

Taylor & Francis
Taylor & Francis Group

ORIGINAL REPORT

OPEN ACCESS

Constitutive modeling of deformation behavior of high-entropy alloys with face-centered cubic crystal structure

Min Ji Jang[a,b], Dong-Hyun Ahn[c], Jongun Moon[a,b], Jae Wung Bae[a,b], Dami Yim[a,b], Jien-Wei Yeh[d], Yuri Estrin[e,f] and Hyoung Seop Kim[a,b]

[a]Department of Materials Science and Engineering, Pohang University of Science and Technology (POSTECH), Pohang, Korea; [b]Center for High Entropy Alloys, Pohang University of Science and Technology (POSTECH), Pohang, Korea; [c]Nuclear Materials Safety Research Division, Korea Atomic Energy Research Institute (KAERI), Daejeon, Korea; [d]Department of Materials Science and Engineering, National Tsing Hua University, Hsinchu, Taiwan; [e]Department of Materials Science & Engineering, Monash University, Clayton, Australia; [f]Laboratory of Nanostructured Hybrid Materials, NUST MISIS, Moscow, Russia

ABSTRACT

A constitutive model based on the dislocation glide and deformation twinning is adapted to face-centered cubic high-entropy alloys (HEAs) as exemplified by the CrMnFeCoNi system. In this model, the total dislocation density is considered as the only internal variable, while the evolution equation describing its variation during plastic deformation is governed by the volume fraction of twinned material. The suitability of the model for describing the strain hardening behavior of HEAs was verified experimentally through compression tests on alloy CrMnFeCoNi and its microstructure characterization by electron backscatter diffraction and X-ray diffraction using synchrotron radiation.
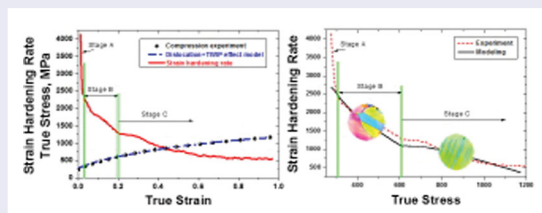
IMPACT STATEMENT

We adopted a constitutive model based on dislocation density and twin volume fraction evolution, to analyze the deformation behavior of the high-entropy alloy CrMnFeCoNi theoretically.

1. Introduction

The advent of high-entropy alloys (HEAs) has changed the paradigm of alloy design, breaking the traditional concept in which an alloy consists of one base metal with added alloying elements [1,2]. By contrast, HEAs are composed of multiple principal elements and form a single phase due to their high-configurational entropy [1]. Despite some controversy around the definition of HEAs, cf. for example, [3,4], the established fact is that the compositional particularity of such systems leads to their exceptional properties. These include high strength due to multiple strengthening mechanisms [5–7], particularly high-temperature strength exceeding that of superalloys [5,8–10], enhanced toughness originating from nano-twins, structural stability [8,10], high-creep resistance

promoted by sluggish diffusion [8,11,12], good weldability [13], large strain hardening capability [6,8], and high-strain rate sensitivity of the flow stress [14]. Furthermore, deformation twinning that occurs in HEAs results in higher strength and better ductility at cryogenic temperatures [2]. In addition, general corrosion resistance of HEAs at room temperature is superior to that of 304S stainless steel [15,16]. Due to these extraordinary properties, HEAs are considered as promising multi-functional materials and the next-generation structural materials.

Among the HEAs, CrMnFeCoNi alloy stands out as a material exhibiting excellent low-temperature mechanical properties [15]. As reported in numerous publications [15,17–22], this is commonly associated with deformation twinning, which causes changes in crystallographic

CONTACT Hyoung Seop Kim ✉ hyoungseopkim@gmail.com

plane orientation that restrict dislocation slip. Deformation twinning in CrMnFeCoNi alloy is generally believed to occur at room temperature, although this was questioned in some reports (cf. [18]). Recent data [13,15,20,23] suggest that twins do occur at sufficiently high strains, when a critical stress for twinning in the alloy (e.g. 720 ± 30 MPa for the HEA reported in [24]) is reached. This is consistent with the experimentally measured and theoretically estimated stacking fault energy of the alloy being low enough to enable twinning [2,25–27]. We have chosen this alloy as a testbed for a constitutive description for HEAs based on a model that considers dislocation glide and deformation twinning. Experimental data required for validation of the model were obtained by compression tests and microstructure analysis. One of the important experimental findings was the observation of the occurrence of deformation twinning at room temperature. A quantitative analysis of the effect of dislocation glide and twinning on plastic strain rate and plastic strain was considered in terms of the theoretical approach developed. A good accord between the experimental data and the predicted evolution of the dislocation density and the twin volume fraction validating the model will be demonstrated below.

2. Materials and methods

For experimental study, a solidified slab of HEA CrMnFeCoNi with a thickness of 11 mm was cold rolled to 5 mm and then annealed at 1100°C for 6 h with subsequent water quenching. Compression tests were performed at room temperature with a constant strain rate of 10^{-3} s^{-1} in an electro-mechanical testing machine (Instron 1361, USA) using cylindrical specimens with diameter of 4.5 mm and height of 4.5 mm. In order to minimize the friction between the surfaces of specimens and anvils, Teflon tape and MoS_2 spray were used as a lubricant. The compressive stress–strain curves were obtained from the data acquired using the digital image correlation technique with an optical 3D deformation analysis system (ARAMIS 5M, GOM Co., Germany).

For characterization of twinning behavior at various strain levels, four specimens were deformed in compression to true strain of 0.13, 0.27, 0.41, and 0.64. Sections of the specimens perpendicular to the direction of compression were mechanically polished with silicon carbide paper of 400, 600, 800, and 1200 grit and diamond suspensions of 3 and 1 μm, then polished to final surface finish with a mixture of 50% ethanol and 50% colloidal silica. The amount of twins in the specimens was evaluated by electron backscatter diffraction (EBSD), which was conducted by using a field emission scanning electron microscope (FE-SEM, Quanta 3D FEG, FEI) equipped with an EBSD system (TSL, TexSEM Laboratory). The EBSD data were interpreted using orientation imaging microscopy software (OIM, TexSEM Laboratory).

In order to investigate microstructural characteristics (dislocation density and twin volume fraction), X-ray diffraction (XRD) analysis was carried out on high-resolution powder diffraction beamline (9B) of the Pohang Light Source in Pohang, Korea. The X-ray radiation was monochromatized to the wavelength of 0.151790 nm by Si (111) double-crystal monochromator. The scan step size was 0.02° with counting time of 10 s, and the flat holder was rotated on the plane of the specimen surface at 60 rotations/min during the scanning time to eliminate any influence of a preferred orientation. The reflected beam was detected by a multiple detector system (7 analyzer crystals + 7 scintillation detectors). XRD patterns were acquired from the surface of the deformed specimens with the four levels of compressive strain and LaB6 powder as a reference peak for convolutional multiple whole profile (CMWP) analyses. The XRD data were analyzed using the CMWP method to obtain microstructural information (dislocation density, dislocation arrangement, crystallite size, twin volume fraction, etc.) from the XRD peak broadening, peak shift, and peak asymmetry [28].

3. Results and discussion

A diagram showing the dependence of the compressive true stress (σ) on the true plastic strain (ε) is presented in Figure 1(a), along with the curve representing the strain dependence of the strain hardening rate $\theta = d\sigma/d\varepsilon$. The stress–strain curve is subdivided into three distinct stages according to the variation of its slope: stage A that extends to a true strain of 0.04 and is characterized by a rapid drop of the strain hardening rate; stage B with a nearly linear decrease of the strain hardening rate with ε that extends to a true strain of 0.2; and, finally, stage C, which holds until the end of straining. To assist the identification of these strain hardening stages, the strain hardening rate is also presented in the Kocks–Mecking plot (θ vs. σ). Using the microstructure data presented below and the shape of the curve in the Kocks–Mecking plot, these three stages can be interpreted as follows. Stage A, in which the strain hardening rate decreases precipitously, corresponds to the elastic–plastic transition. This is followed by a gradual decrease in the strain hardening rate in stage B, which can be associated with plastic deformation governed by dislocation glide. The linear character of this stage in the θ vs. σ diagram in Figure 1(b) suggests that it can be identified with stage III behavior observed in most conventional alloys, which is controlled by the dynamic recovery of dislocations [29]. With further straining,
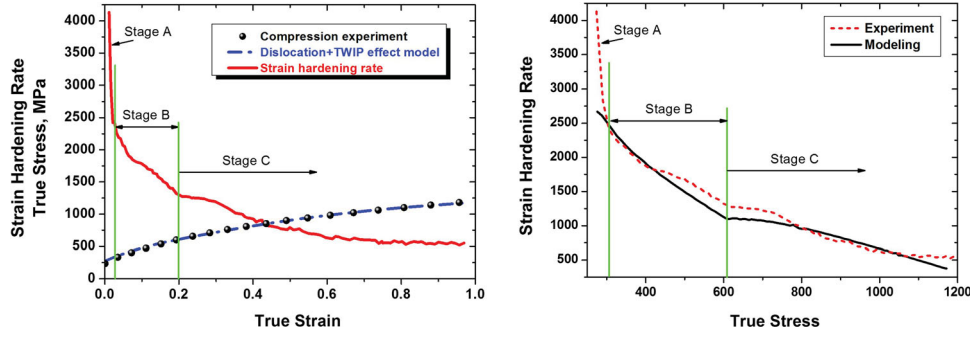
Figure 1. (a) Experimental strain dependence of the true stress and the strain hardening rate for uniaxial compression, and the stress–strain curve predicted by the model proposed in this paper; (b) strain hardening curves in the Kocks–Mecking plot (θ vs. σ).

mechanical twinning is generated, resulting in a boost in strain hardening (stage C). It interrupts the linear decline of the strain hardening rate seen in stage B and delays the asymptotic approach to zero strain hardening (steady state).

Under the premise that interplay between dislocation slip and deformation twinning in the CrMnFeCoNi HEA is not dissimilar to that in twinning induced plasticity (TWIP) steels, we adapted a constitutive model that proved to be successful in describing the deformation behavior of TWIP steels. The model goes back to the classical approach of Kocks and Mecking [29] and combines the elements of the models of Bouaziz et al. [30] and Ahn et al. [31]. The resulting set of constitute relations made it possible to account for the evolution of the dislocation density and the twin volume fraction obtained experimentally.

The model relates the flow stress σ to the total dislocation density ρ through the Taylor equation, where the flow stress is proportional to the square root of the dislocation density:

$$\sigma = \sigma_0 + \alpha MGb\sqrt{\rho}, \qquad (1)$$

where σ_0 is a 'friction stress' necessary to activate dislocation glide, α is a numerical constant, M is the Taylor factor accounting for texture, G is the shear modulus, and b is the magnitude of the Burgers vector. The equation indicates that a higher flow stress for dislocation glide is required with increasing dislocation density, as the dislocation mean free path, which is proportional to $1/\sqrt{\rho}$, becomes shorter.

The evolution of the dislocation density with shear strain γ_g associated with dislocation glide is described by the Kocks–Mecking–Estrin equation [32]:

$$\frac{d\rho}{d\gamma_g} = \frac{1}{bL} + \frac{k}{b}\sqrt{\rho} - f\rho, \qquad (2)$$

where the first term on the right-hand side is associated with dislocation storage at obstacles extraneous to dislocation structure (having a spacing L) and the second term accounts for dislocation storage at dislocation-related obstacles (such as, e.g. dislocation cell walls); the rate of this athermal storage is controlled by the coefficient k. Finally, the last term is related to the dynamic recovery by dislocation annihilation, with f denoting the dynamic recovery coefficient.

In the case considered, where the obstacles to dislocation motion are mainly associated by grain boundaries and twin boundaries, the obstacle spacing L is given by

$$\frac{1}{L} = \frac{1}{d} + \frac{1}{t}, \qquad (3)$$

where d is the average grain size and t is the mean twin spacing. Following Bouaziz et al. [30], we relate the quantity t to the average twin thickness e and twin volume fraction F [30]:

$$t = 2e \cdot \frac{1 - F}{F}. \qquad (4)$$

This equation reflects a 'dynamic' Hall–Petch relation: as F increases during deformation, L drops off, which leads to an enhancement of dislocation storage. Accordingly, deformation twinning promotes strain hardening.

The variation of the twin volume fraction F in the strain range above the twinning onset strain ε_0 is taken in the form of an *ansatz* involving an error function *erf*, which is a heuristic law used in the absence of a more physically based expression [30]:

$$F = F_0 + (F_\infty - F_0) \times \text{erf}\left(\frac{\varepsilon - \varepsilon_0}{\tilde{\varepsilon}}\right), \qquad (5)$$

where F_0 is the initial twin volume fraction at $\varepsilon = \varepsilon_0$, F_∞ is a saturation value of F, and $\tilde{\varepsilon}$ is a parameter governing the rate of evolution of the twin volume fraction with the axial strain ε.

The shear strain γ is related to the axial strain ε via

$$\gamma = M\varepsilon, \tag{6}$$

where M is the Taylor factor accounted for the texture of the material. A plastic strain increment comprises both dislocation glide and twinning parts. Accordingly, the differential of the shear strain is represented by a rule of mixtures with the contributions from dislocation glide and twinning:

$$d\gamma = (1 - F) \cdot d\gamma_g + \gamma_t \cdot dF, \tag{7}$$

where γ_t is the twinning shear strain, which is equal to $1/\sqrt{2}$ [30]. The first and second terms on the right-hand side of the equation represent dislocation glide and twinning contributions, respectively.

The above set of equations, Equations (1)–(7), provide a complete constitutive description for the alloy. Some of the parameters entering the model equations were fixed: $\alpha = 0.33$, $M = 3.06$, $G = 81\,\text{GPa}$, $b = 0.254\,\text{nm}$, $d = 52\,\mu\text{m}$, $e = 0.01\,\mu\text{m}$ [33], and $F_0 = 0$. The rest were determined using experimental data and applying a genetic algorithm for parameter identification [33,34]. The following set of parameters was obtained in this way: $\sigma_0 = 210\,\text{MPa}$, $F_\infty = 0.012$, $\varepsilon_0 = 0.2$, $\tilde{\varepsilon} = 1$, $k = 0.018$, and $f = 2.128$. The HEA CrMnFeCoNi was found to have a higher k value and a lower f value than 304 L steel and high-Mn steel [35]. The k value reflects the efficacy of the dislocation structure in storing dislocations, and therefore, this storage mechanism is more efficient in HEA CrMnFeCoNi than in the mentioned steels: $k = 0.011$ for 304 L and high-Mn steel [35,36]. The lower f value means that the rate of dynamic recovery is slower in the HEA than in 304 L and high-Mn steel for which $f = 3$ was found [35]. It may be conjectured that the high strength of dislocation-related obstacles on which dislocation storage occurs and the low rate of dynamic recovery are attributable to strong crystal lattice distortion, which is caused by multiple principal elements with different atomic radii.

The dislocation-based model considered also provides access to the evolution of the dislocation density. The variation of ρ theoretically predicted by the model and measured experimentally using the CMWP method is presented in Figure 2. It is obvious that the twinning component of the model gives rise to a greater dislocation density and enhanced strain hardening due to dislocation storage at twin boundaries (dynamic Hall–Petch effect) [26]. The model calculations match the evolution of the dislocation density monitored at four levels of compressive strain by means of CMWP fitting qualitatively, although the model underpredicts the magnitude of ρ.
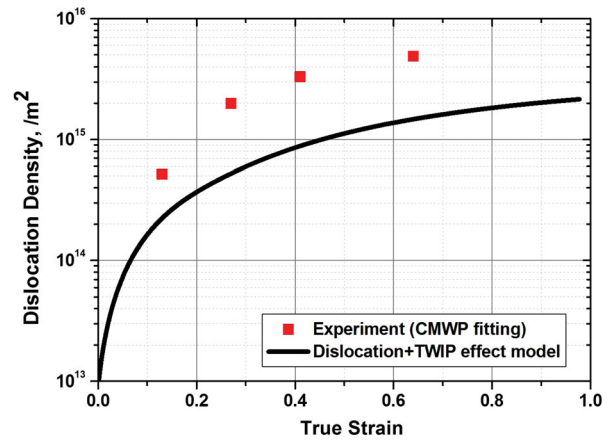

Figure 2. Strain dependence of the dislocation density predicted using the proposed model and measured by the CMWP fitting of the synchrotron XRD peaks.
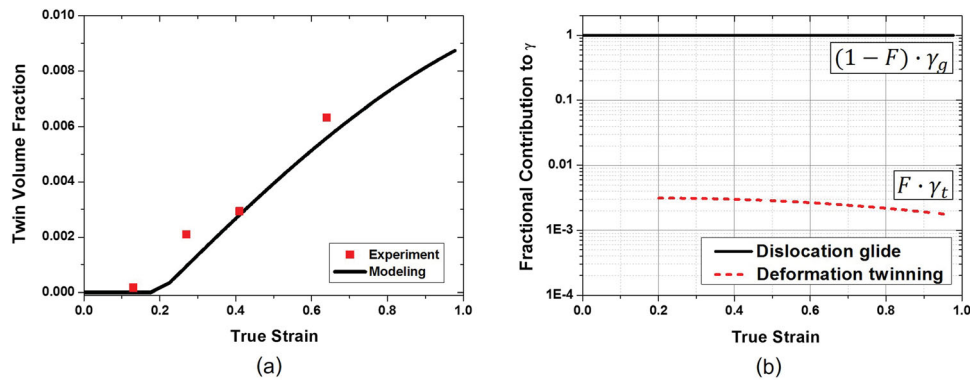
The evolution of the twin volume fraction was assessed using EBSD measurements. The EBSD inverse pole figure (IPF) map in Figure 3(a) for the lowest true strain considered (0.13) corresponds to microstructure with annealing twins only, before the initiation of deformation twinning. The IPF maps after compression in Figure 3(b,d) and their enlarged views in Figure 3(c,e) show that after 27% strain, deformation twinning has occurred in a small fraction of grains. After 41% strain, deformation twin bundles are commonly found. In other words, the number of twinned grains and the volume fraction of twins within those grains go up with increasing strain. Apparently, deformation twinning sets in at a certain true strain between 0.13 and 0.27, which can be regarded as an end of stage B of strain hardening (i.e. stage III in the conventional nomenclature). From then on, deformation twinning starts contributing to strain hardening, thus decelerating the decrease of the strain hardening rate and approach of steady state.

In our constitutive description, the evolution of the twin volume fraction, $F(\varepsilon)$, is represented by the black solid line in Figure 4(a). It starts growing at the twinning initiation point ($\varepsilon = 0.2$), and follows Equation (5). The function $F(\varepsilon)$ was also measured experimentally using CMWP fitting. The measurement results are in good quantitative agreement with those given by Equation (5). In addition, the individual contributions of dislocation glide and deformation twinning to the shear strain γ were analyzed. The results presented in Figure 4(b) show that the dislocation glide contribution is in excess of 99.5%. That is to say, deformation twinning contributes to shear strain only marginally, and its main role consists in restricting the deformation mean free path, thus affecting the strain hardening rate via a dynamic Hall–Petch effect.
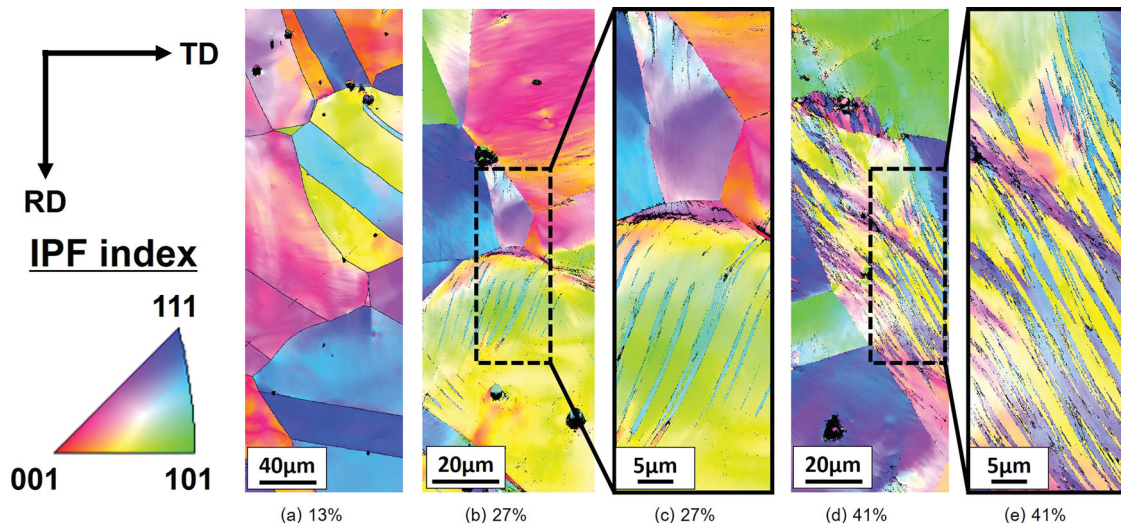
Figure 3. EBSD IPF maps for specimens deformed in compression to various strains: (a) 13%, (b) 27%, (d) 41%; figures (c) and (e) show enlarged images of (b) and (d), respectively.

Figure 4. (a) The evolution of the twin volume fraction f according to the model and measured experimentally by CMWP fitting; (b) fractional contribution of dislocation glide and deformation twinning to shear strain.

The stress–strain curve calculated on this basis fits the experimental one very well, as shown in Figure 1. It should be emphasized that not only the experimental stress–strain curve is matched by the calculated curve as shown in Figure 1(a). The variation of the *derivative* of stress with respect to strain, represented by the calculated strain hardening rate, which is by far more sensitive to model details, is in good accord with the experimental curve as well, cf. Figure 1(b). Thus, it can be stated with confidence that the constitutive framework outlined in this article enables a sufficient level of fidelity and predictive ability of the model.

4. Conclusions

In summary, we adopted a constitutive model based on dislocation density and twin volume fraction evolution, to analyze the deformation behavior of the HEA CrMnFeCoNi theoretically. The model was validated by experimental data obtained for the alloy. In particular, the stress–strain curve obtained for the room temperature deformation in compression was well described by the model. In addition, the dislocation density and the twin volume fraction determined experimentally using the CMWP fitting and EBSD mapping were shown to be in good agreement with model predictions. The results demonstrated that dislocation glide is the primary deformation mechanism, while deformation twinning influences the deformation behavior indirectly, through its effect on the strain hardening, particularly at later stages of straining. The model makes an accurate prediction of the deformation behavior and microstructure evolution of HEA CrMnFeCoNi. It is expected to have a more general validity for HEAs and not only to the specific HEA considered here.

Acknowledgements

Disclosure statement

No potential conflict of interest was reported by the authors.

Funding

References

[1] Yeh JW, Chen SK, Lin SJ, et al. Nanostructured high-entropy alloys with multiple principal elements: novel alloy design concepts and outcomes. Adv Eng Mater. 2004;6(5):299–303.

[2] Yeh JW. Physical metallurgy of high-entropy alloys. J Miner. 2015;67(10):2254–2261.

[3] Zhang Y, Guo S, Liu C, et al. Phase formation rules. In: Gao MC, Yeh JW, Liaw PK, Zhang Y, editors. High-entropy alloys. Aargau (CH): Springer; 2016. p. 21–49.

[4] Tomilin IA, Kaloshkin SD. 'High entropy alloys'—'semi-impossible'regular solid solutions? Mater Sci Tech. 2015; 31(10):1231–1234.

[5] Zhang Y, Zuo TT, Tang Z, et al. Microstructures and properties of high-entropy alloys. Prog Mater Sci. 2014;61:1–93.

[6] Park N, Watanabe I, Terada D, et al. Recrystallization behavior of CoCrCuFeNi high-entropy alloy. Metall Mater Trans A. 2015;46(4):1481–1487.

[7] Park N, Li X, Tsuji N. Microstructure and mechanical properties of $Co_{21}Cr_{22}Cu_{22}Fe_{21}Ni_{14}$ processed by high pressure torsion and annealing. J Mater. 2015;67(10): 2303–2309.

[8] Tsai MH, Yeh JW. High-entropy alloys: a critical review. Mater Res Lett. 2014;2(3):107–123.

[9] Senkov ON, Wilks GB, Scott JM, et al. Mechanical properties of $Nb_{25}Mo_{25}Ta_{25}W_{25}$ and $V_{20}Nb_{20}Mo_{20}Ta_{20}W_{20}$ refractory high entropy alloys. Intermetallics. 2011;19(5): 698–706.

[10] Pickering EJ, Muñoz-Moreno R, Stone HJ, et al. Precipitation in the equiatomic high-entropy alloy CrMnFeCoNi. Scripta Mater. 2016;113:106–109.

[11] Woo W, Huang EW, Yeh JW, et al. In-situ neutron diffraction studies on high-temperature deformation behavior in a CoCrFeMnNi high entropy alloy. Intermetallics. 2015;62:1–6.

[12] Lee DH, Seok MY, Zhao Y, et al. Spherical nanoindentation creep behavior of nanocrystalline and coarse-grained CoCrFeMnNi high-entropy alloys. Acta Mater. 2016;109:314–322.

[13] Wu Z, David SA, Feng Z, et al. Weldability of a high entropy CrMnFeCoNi alloy. Scripta Mater. 2016;124: 81–85.

[14] Lee DH, Choi IC, Seok MY, et al. Nanomechanical behavior and structural stability of a nanocrystalline CoCrFeNiMn high-entropy alloy processed by high-pressure torsion. J Mater Res. 2015;30(18):2804–2815.

[15] Gludovatz B, Hohenwarter A, Catoor D, et al. A fracture-resistant high-entropy alloy for cryogenic applications. Science. 2014;345(6201):1153–1158.

[16] Chen YY, Duval T, Hung UD, et al. Microstructure and electrochemical properties of high entropy alloys—a comparison with type-304 stainless steel. Corros Sci. 2005;47(9):2257–2279.

[17] Deng Y, Tasan CC, Pradeep KG, et al. Design of a twinning-induced plasticity high entropy alloy. Acta Mater. 2015;94:124–133.

[18] Otto F, Dlouhý A, Somsen C, et al. The influences of temperature and microstructure on the tensile properties of a CoCrFeMnNi high-entropy alloy. Acta Mater. 2013;61(15):5743–5755.

[19] Otto F, Hanold NL, George EP. Microstructural evolution after thermomechanical processing in an equiatomic, single-phase CoCrFeMnNi high-entropy alloy with special focus on twin boundaries. Intermetallics. 2014;54: 39–48.

[20] Stepanov N, Tikhonovsky M, Yurchenko N, et al. Effect of cryo-deformation on structure and properties of CoCrFeNiMn high-entropy alloy. Intermetallics. 2015;59: 8–17.

[21] Tsai CW, Chen YL, Tsai MH, et al. Deformation and annealing behaviors of high-entropy alloy Al0.5 CoCrCuFeNi. J Alloy Compd. 2009;486(1–2):427–435.

[22] Gali A, George EP. Tensile properties of high- and medium-entropy alloys. Intermetallics. 2013;39:74–78.

[23] Schuh B, Mendez-Martin F, Völker B, et al. Mechanical properties, microstructure and thermal stability of a nanocrystalline CoCrFeMnNi high-entropy alloy after severe plastic deformation. Acta Mater. 2015;96:258–268.

[24] Laplanche G, Kostka A, Horst O, et al. Microstructure evolution and critical stress for twinning in the CrMnFeCoNi high-entropy alloy. Acta Mater. 2016;118: 152–163.

[25] Zaddach AJ, Niu C, Koch CC, et al. Mechanical properties and stacking fault energies of NiFeCrCoMn high-entropy alloy. J Mater. 2013;65(12):1780–1789.

[26] Huang S, Li W, Lu S, et al. Temperature dependent stacking fault energy of FeCrCoNiMn high entropy alloy. Scripta Mater. 2015;108:44–47.

[27] Sathiaraj GD, Bhattacharjee PP. Analysis of microstructure and microtexture during grain growth in low stacking fault energy equiatomic CoCrFeMnNi high entropy and Ni–60wt.%Co alloys. J Alloy Compd. 2015;637:267–276.

[28] Ungár T. Microstructural parameters from X-ray diffraction peak broadening. Scripta Mater. 2004;51(8):777–781.

[29] Kocks UF, Mecking H. Physics and phenomenology of strain hardening: the FCC case. Prog Mater Sci. 2003;48(3):171–273.

[30] Bouaziz O, Allain S, Scott CP, et al. High manganese austenitic twinning induced plasticity steels: a review of the microstructure properties relationships. Curr Opin Solid State Mater Sci. 2011;15(4):141–168.

[31] Ahn DH, Kim HS, Estrin Y. A semi-phenomeno-logical constitutive model for hcp materials as exemplified by alpha titanium. Scripta Mater. 2012;67(2):121–124.

[32] Estrin Y, Mecking H. A unified phenomenological description of work hardening and creep based on one-parameter models. Acta Metall. 1984;32(1):57–70.

[33] Wu Z, Parish CM, Bei H. Nano-twin mediated plasticity in carbon-containing FeNiCoCrMn high entropy alloys. J Alloy Compd. 2015;647:815–822.

[34] Laplanche G, Gadaud P, Horst O, et al. Temperature dependencies of the elastic moduli and thermal expansion coefficient of an equiatomic, single-phase CoCrFeMnNi high-entropy alloy. J Alloy Compd. 2015;623:348–353.

[35] Bouaziz O, Guelton N. Modelling of TWIP effect on work-hardening. Mater Sci Eng A. 2001;319–321:246–249.

[36] Kang JH, Ingendahl T, Bleck W. A constitutive model for the tensile behaviour of TWIP steels: composition and temperature dependencies. Mater Des. 2016;90:340–309.